Multiresolution schemes for conservation laws

Siegfried Müller

Abstract The concept of fully adaptive multiresolution finite volume schemes has been developed and investigated during the past decade. By now it has been successfully employed in numerous applications arising in engineering. In the present work a review on the methodology is given that aims to summarize the underlying concepts and to give an outlook on future developments.

1 Introduction

Nowadays scientific computing has become an indispensable tool in engineering. For instance, numerical simulations of fluid flow can help to shorten the development cycle of new airplanes. In the near future, it might be even possible to perform real-time simulations of flying airplanes, to determine aerodynamical loads for the entire flight regime, to numerically predict the performance and the flight quality of an airplane before the maiden flight, as well as to do the certification before the airplane construction on the basis of numerical data. These are the challenging goals of the new Center for Computer Applications in Aerospace Science and Engineering ($C^2A^2S^2E$) funded in 2007 at the DLR Braunschweig.

Typically the numerical simulation of such real-world applications requires meshes with several millions of cells. This poses enormous challenges to computing resources and data management strategies. Improved hardware or purely data oriented strategies such as parallel computing are not sufficient to overcome the arising difficulties. In the long run, they have to be complemented by mathematical concepts that aim at minimizing the size of the resulting discrete problems and, thus, to keep the computational complexity tractable. One promising approach in

Siegfried Müller
Institut für Geometrie und Praktische Mathematik, RWTH Aachen University, D-52056 Aachen, Germany, e-mail: mueller@igpm.rwth-aachen.de

R.A. DeVore, A. Kunoth (eds.), *Multiscale, Nonlinear and Adaptive Approximation*,
DOI 10.1007/978-3-642-03413-8_11,

this direction is based on local grid adaptation which aims to adjust the resolution of the discretization to the local regularity of the underlying solution.

This paper summarizes some recent work on grid adaptation in the context of hyperbolic conservation laws that arise, for instance, from the balance equations derived in continuum mechanics and modeling fluid flow. Currently, several different adaptive concepts for conservation laws are being discussed and investigated in the literature. A standard approach is based on error indicators, for instance gradient-based indicators [10, 8] or local residuals [43, 66, 67]. In practice, these approaches turned out to be very efficient. However, the error indicator is highly case dependent, i.e., it needs a lot of parameter tuning to avoid excessive mesh growth or missing refinement of important flow features. In particular, it does not estimate the local discretization error and, hence, it provides no reliable error control. Here a-posteriori error estimators offer an alternative that aims at the equidistribution of the error, cf. [48]. These rely on L^1-error-estimates. In particular, they are based on Kruzkov's entropy condition [49] and Kuznetsov's a-priori estimates [50] that are only available for scalar multidimensional conservation laws. If only a functional of the solution is of interest rather than the solution in the entire flow field, then another approach is of interest based on the solution of an adjoint problem [5, 42, 70, 69]. Here grid adaptation is tuned with respect to the efficient and accurate computation of a target quantity, e.g. drag or lift. Since this approach requires to store to some extent the time history of the evolution, this certainly poses a considerable challenge to computational resources in case of 3D unsteady problems.

In recent years, the new concept of multiscale-based grid adaptation has been developed and applied to complex multidimensional flow problems. The main distinction from previous work lies in the fact that we employ *multiresolution techniques*. The starting point is a proposal by Harten [38] to transform the arrays of cell averages associated with any given finite volume discretization of the underlying conservation laws into a different format that reveals insight into the local behavior of the solution. The cell averages on a given highest level of resolution (*reference mesh*) are represented as cell averages on some coarse level where the fine scale information is encoded in arrays of *detail coefficients* of ascending resolution. This requires a *hierarchy of meshes*.

In Harten's original approach [39, 40, 12], the multiscale analysis is used to control a hybrid flux computation which can save CPU time for the flux evaluation. However, the overall computational complexity is not reduced but still stays proportional to the number of cells on the uniformly fine reference mesh which in 3D calculations is prohibitive. Alternatively to this strategy, threshold techniques are applied to the multiresolution decomposition in [54, 25], where detail coefficients below a threshold value are discarded. By means of the remaining significant details, a locally refined mesh is determined whose complexity is significantly reduced in comparison to the underlying reference mesh. Thus a principal objective is to extract the inherent complexity of the problem by placing as few degrees of freedom as possible while the features of the solution are still captured within a given tolerance. A central mathematical problem is to show that the essential information to be propagated in time is still kept with sufficient accuracy when working on locally

coarser meshes. This has been proven for scalar onedimensional conservation laws in [25, 44].

The fully adaptive concept has turned out to be highly efficient and reliable. So far, it has been applied with great success to different applications, e.g., 2D/3D–steady and unsteady computations of compressible fluids around airfoils modeled by the Euler and Navier–Stokes equations, respectively, on block–structured curvilinear grid patches [15], backward–facing step on 2D triangulations [26] and simulation of a flame ball modeled by reaction–diffusion equations on 3D Cartesian grids [63]. These applications have been performed for compressible single-phase fluids. More recently, this concept has been extended to two-phase fluid flow of compressible gases, and applied to the investigation of non–stationary shock–bubble interactions on 2D Cartesian grids for the Euler equations [1, 55]. By now, there are several groups working on this subject: Postel et al. [28], Schneider et al. [61, 62], Bürger et al. [20, 19] and Domingues et al. [30].

The aim of the present work is to give an overview on the concept of multiscale-based grid adaptation. For this purpose, we first summarize the basic ingredients of the grid adaptation concept starting with the underlying equations and their discretization using finite volume schemes, see Section 2. This is followed by the multiscale analysis of the discrete cell averages resulting from the finite volume discretization, see Section 3, and the construction of locally refined grids using data compression techniques, see Section 4. Applying the multiscale analysis to the original finite volume discretization on the uniform grid we obtain multiscale evolution equations, see Section 5. The crucial point is then to perform the time evolution on the adaptive grid where the accuracy of the uniform discretization is maintained but the computational complexity is proportional only to the number of cells of the adaptive grid, see Section 5.5. For this purpose, the computation of the local flux balances and sources has to be performed judiciously, see Section 5.2, and the adaptive grid has to be predicted appropriately from the data of the previous time step, see Section 5.3. The resulting adaptive multiresolution scheme is further accelerated using multilevel time stepping strategies, see Section 5.4. In order to confirm that the multiresolution grid adaptation concept can deal with challenging applications in engineering, we present in Section 6 numerical simulations of two vortices generated at an airplane wing and moving in the wake of the airplane. The computations have been performed with the adaptive, parallel Quadflow solver [15]. In Section 7, we conclude with some remarks on future trends of adaptive multiresolution schemes.

2 Governing equations and finite volume schemes

The fluid equations are determined by the balance equations

$$\frac{\partial}{\partial t}\int_V \mathbf{u}\ dV + \oint_{\partial V} \mathbf{f}(\mathbf{u})\cdot\mathbf{n}\ dS = \int_V \mathbf{s}(\mathbf{u})\ dV\,, \tag{1}$$

where $\mathbf{u}$ is the array of the mean conserved quantities, e.g., density of mass, momentum, specific total energy, $\mathbf{f}$ is the array of the corresponding convective and diffusive fluxes, and $\mathbf{s}$ denotes a source term that may occur, for instance, in turbulence modeling. For simplicity of representation, we will always assume that V is time-independent. In principle, the concepts presented below can easily be extended to moving boundaries, cf. [15, 52].

The balance equations (1) are approximated by a finite volume scheme. For this purpose the finite fluid domain $\Omega \subset \mathbf{R}^d$ is split into a finite set of subdomains, the cells V_i, such that all V_i are disjoint and their union covers Ω. According to our simplifying assumption, the grid does not move in time. Furthermore let $N(i)$ be the set of cells that have a common edge with the cell i, and for $j \in N(i)$ let $\Gamma_{ij} := \partial V_i \cap \partial V_j$ be the interface between the cells i and j and $\mathbf{n}_{ij}$ the outer normal of Γ_{ij} corresponding to the cell i. In time we use a global time step τ^n for all cells that might change due to the Courant-Friedrich-Levy (CFL) condition, i.e., $t^{n+1} = t^n + \tau^{n+1}$, $t^0 = 0$. For the time discretization in (1) we confine to an explicit time discretization of the approximated cell averages $v_i^n \approx |V_i|^{-1} \int_{V_i} u(t^n, x)\, dx$ that can be written in the form

$$v_i^{n+1} = v_i^n - \frac{\tau_i^{n+1}}{|V_i|} (B_i^n + |V_i| S_i^n). \tag{2}$$

By this discrete evolution equation the approximated cell averages of the conserved variables are updated on the new time step. Here the fluxes and the source terms are approximated by

$$B_i^n := \sum_{j \in N(i)} |\Gamma_{ij}| F(v_{ij}^n, v_{ji}^n, \mathbf{n}_{ij}), \quad S_i^n := S(v_i^n), \tag{3}$$

where the numerical flux function $F(\mathbf{u}, \mathbf{w}, \mathbf{n})$ is an approximation for the flux $f(\mathbf{u}, \mathbf{n}) := \mathbf{f} \cdot \mathbf{n}$ in outer normal direction $\mathbf{n}_{ij}$ on the edge Γ_{ij}. The numerical flux is assumed to be *consistent*, i.e., $F(\mathbf{u}, \mathbf{u}, \mathbf{n}) = f(\mathbf{u}, \mathbf{n})$. For simplicity of presentation we neglect the fact that, due to higher order reconstruction, F usually depends on an enlarged stencil of cell averages. Moreover, to preserve a constant flow field we assume that the geometric consistency condition $\sum_{j \in N(i)} |\Gamma_{ij}| \mathbf{n}_{ij} = \mathbf{0}$ holds. This condition is easy to satisfy in case of planar faces. However, for more general discretizations, e.g. curvilinear grid patches [51], it imposes a constraint on the approximation of the normal vector $\mathbf{n}_{ij}$.

We want to remark that the finite volume discretization (2) is just a simplified prototype. More advanced discretizations can be considered where (i) the time discretization is replaced by some implicit scheme, cf. [15, 56, 57], or a Runge-Kutta scheme, cf. [63], (ii) the time stepsize is changing locally for each cell, cf. [15, 56], and (iii) the source term approximation is based on some higher order approximation.

3 Multiscale analysis

A finite volume discretization typically works on an array of cell averages. In order to realize a certain target accuracy at the expense of a possibly low number of degrees of freedom, viz. a possibly low computational effort, one should keep the size of the cells large wherever the data exhibit little variation, reflecting a high regularity of the searched solution components. Our analysis of the local regularity behavior of the data is based on the concept of biorthogonal wavelets [21]. This approach may be seen as a natural generalization of Harten's discrete framework [41]. The core ingredients are (i) a hierarchy of nested grids, (ii) biorthogonal wavelets and (iii) the multiscale decomposition. In what follows we will only summarize the basic ideas. For the realization and implementation see [54].

Grid hierarchy. Let $\Omega_l := \{V_\lambda\}_{\lambda \in I_l}$ be a sequence of different meshes corresponding to different resolution levels $l \in \mathbf{N}_0$, where the mesh size decreases with increasing refinement level. The grid hierarchy is assumed to be *nested*. This implies that each cell $\lambda \in I_l$ on level l is the union of cells $\mu \in M_\lambda^0 \subset I_{l+1}$ on the next higher refinement level $l+1$, i.e.,

$$V_\lambda = \bigcup_{\mu \in M_\lambda^0 \subset I_{l+1}} V_\mu, \quad \lambda \in I_l, \tag{4}$$

where $M_\lambda^0 \subset I_{l+1}$ is the refinement set. A simple example is shown in Figure 1 for a dyadic grid refinement of Cartesian meshes. Note that the framework presented here is not restricted to this simple configuration but can also be applied to *unstructured* grids and *irregular* grid refinements, cf. [54].

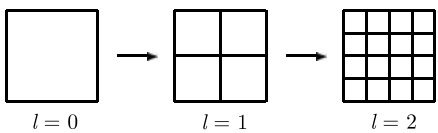

Fig. 1 Sequence of nested grids

Example. In the sequel, the concept will be illustrated for 1D dyadic grid refinements on the real axis. Then a nested grid hierarchy is determined by $\mathscr{G}_l := \{V_{l,k}\}_{k \in I_l}$, $l \in \mathbf{N}_0$, $I_l = \mathbf{Z}$. These meshes are composed of the intervals $V_{l,k} = [x_{l,k}, x_{l,k+1}]$ determined by the grid points $x_{l,k} = 2^{-l}k$, $k \in I_l$, with interval length $h_l = 2^{-l}$. Due to the subdivision $V_{l,k} = V_{l+1,2k} \cup V_{l+1,2k+1}$ the refinement set is determined by $M_{l,k}^0 = \{2k, 2k+1\}$. Here the index λ is identified by (l,k).

Box function and cell averages. With each cell V_λ in the partitions Ω_l we associate the so–called *box function*

$$\tilde{\phi}_\lambda(x) := \frac{1}{|V_\lambda|}\chi_{V_\lambda}(x) = \begin{cases} 1/|V_\lambda|, & x \in V_\lambda \\ 0, & x \notin V_\lambda \end{cases}, \quad \lambda \in I_l \tag{5}$$

defined as the L^1–normalized characteristic function of V_λ. By $|V|$ we denote the volume of a cell V. Then the averages of a scalar, integrable function $u \in L^1(\Omega)$ can be interpreted as an inner product, i.e.,

$$\hat{u}_\lambda := \langle u, \tilde{\phi}_\lambda \rangle_\Omega \quad \text{with} \quad \langle u, v \rangle_\Omega := \int_\Omega u\, v\, dx. \tag{6}$$

Obviously, the nestedness of the grids as well as the linearity of integration imply the two–scale relations

$$\tilde{\phi}_\lambda = \sum_{\mu \in M_\lambda^0 \subset I_l} m_{\mu,\lambda}^{l,0}\, \tilde{\phi}_\mu \quad \text{and} \quad \hat{u}_\lambda = \sum_{\mu \in M_\lambda^0 \subset I_l} m_{\mu,\lambda}^{l,0}\, \hat{u}_\mu, \quad \lambda \in I_{l-1}, \tag{7}$$

where the mask coefficients turn out to be $m_{\mu,\lambda}^{l,0} := |V_\mu|/|V_\lambda|$ for each cell $\mu \in M_\lambda^0$ in the refinement set.

Example. In case of the 1D dyadic grid refinement the box function is just $\tilde{\phi}_{l,k}(x) := 2^{-l}$ for $x \in V_{l,k}$ and zero elsewhere, see Figure 2 (left). The corresponding mask coefficients are $m_{r,k}^{l,0} := |V_{l+1,r}|/|V_{l,k}| = 0.5$ for $r \in M_{l,k}^0 \subset I_{l+1}$, $k \in I_l$. For a general grid hierarchy the mask coefficients may depend on the level and the position.

Wavelets and details. In order to detect singularities of the solution we consider the difference of the cell averages corresponding to different resolution levels. For this purpose we introduce the wavelet functions $\tilde{\psi}_\lambda$ as linear combinations of the box functions, i.e.,

$$\tilde{\psi}_\lambda := \sum_{\mu \in M_\lambda^1 \subset I_{l+1}} m_{\mu,\lambda}^{l,1}\, \tilde{\phi}_\mu, \quad \lambda \in J_l, \tag{8}$$

with mask coefficients $m_{\mu,\lambda}^{l,1}$ that only depend on the grids. Here the wavelet functions $\tilde{\Psi}_l := (\tilde{\psi}_\lambda)_{\lambda \in J_l}$ build an appropriate completion of the basis system $\tilde{\Phi}_l := (\tilde{\phi}_\lambda)_{\lambda \in I_l}$. By this we mean (i) they are locally supported, (ii) provide vanishing moments of a certain order and (iii) there exists a biorthogonal system Φ_l and Ψ_l of primal functions satisfying two-scale relations similar to (7) and (8). The last requirement is typically the hardest to satisfy. It is closely related to the Riesz basis property of the infinite collection $\tilde{\Phi}_0 \cup \bigcup_{l=0}^\infty \tilde{\Psi}_l$ of $L_2(\Omega)$. For details we refer to the *concept of stable completions*, see [21].

Aside from these stability aspects, the biorthogonal framework allows for an efficient change of basis. While the relations (7) and (8) provide expressions of the coarse scale box functions and detail functions as linear combinations of fine scale box functions, the mask coefficients in the analogous two-scale relations for the dual system Φ_l, Ψ_l give rise to the reverse change of basis between $\tilde{\Phi}_l \cup \tilde{\Psi}_l$ and $\tilde{\Phi}_{l+1}$, i.e.,

$$\tilde{\phi}_\lambda = \sum_{\mu \in G_\lambda^0 \subset I_l} g_{\mu,\lambda}^{l,0}\, \tilde{\phi}_\mu + \sum_{\mu \in G_\lambda^1 \subset J_l} g_{\mu,\lambda}^{l,1}\, \tilde{\psi}_\mu, \quad \lambda \in I_{l+1}, \tag{9}$$

where we rewrite the basis function $\tilde{\phi}_\lambda$ on level $l+1$ by the scaling functions $\tilde{\phi}_\mu$ and the wavelet functions $\tilde{\psi}_\mu$ on the next coarser scale l. Here again the mask coefficients $g^{l,0}_{\mu,\lambda}$ and $g^{l,1}_{\mu,\lambda}$ depend only on the grid geometry.

Biorthogonality also yields a data representation in terms of the primal system Ψ. The expansion coefficients d_λ with respect to the basis Ψ are obtained by testing u with the elements from $\tilde{\Psi}$, i.e.,

$$d_\lambda := \langle u, \tilde{\psi}_\lambda \rangle_\Omega = \sum_{\mu \in M^1_\lambda} m^{l,1}_{\mu,\lambda}\, \hat{u}_\mu, \quad \lambda \in J_l. \tag{10}$$

These are referred to as the *detail coefficients*. Their two-scale format follows from the functional counterpart of (8).

Note that the dual system $\tilde{\Psi}$ is used to expand the cell averages which are *functionals* of the solution u whose propagation in time gives rise to the finite volume scheme. The primal basis itself will actually never be used to represent the solution u. Instead, the enhanced accuracy of the approximate cell averages can be used for higher order reconstructions commonly used in finite volume schemes.

Example. In case of the 1D dyadic grid refinement, the L^1-normalized Haar wavelet $\tilde{\psi}^H_{l,k} := (\tilde{\phi}_{l+1,2k} + \tilde{\phi}_{l+1,2k+1})/2$ can be used, see Figure 2 (middle). The corresponding mask coefficients are $m^{l,1}_{r,k} := 0.5$ for $r \in M^1_{l,k} \equiv M^0_{l,k} \subset I_{l+1}$, $k \in I_l$. For a general grid hierarchy the mask coefficients may depend on the level and the position.

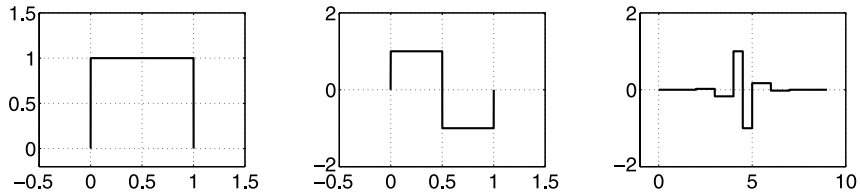

Fig. 2 Box function $\tilde{\phi}_{0,0}$ (left), Haar wavelet $\tilde{\psi}^H_{0,0}$ (middle), and modified Haar wavelet $\tilde{\psi}_{0,0}$ with $s = 2$ (right)

Cancellation Property. It can be shown that the details become small with increasing refinement level when the underlying function is smooth

$$|d_\lambda| \le C 2^{-lM} \|u^{(M)}\|_{L^\infty(V_\lambda)} \tag{11}$$

in the support of the wavelet $\tilde{\psi}_\lambda$. More precisely, the details decay at a rate of at least 2^{-lM}, provided that the function u is sufficiently differentiable and the wavelets have vanishing moments of order M, i.e.,

$$\langle p, \tilde{\psi}_\lambda \rangle_\Omega = 0 \tag{12}$$

for all polynomials p of degree less than M. Here we assume that the grid hierarchy is quasi-uniform in the sense that the diameters of the cells on each level l are proportional to 2^{-l}.

If coefficient and function norms behave essentially the same, as asserted by the Riesz basis property, (11) suggests to neglect all sufficiently small details in order to compress the original data. In fact, the higher M the more details may be discarded in smooth regions.

Example. The Haar wavelet has only one vanishing moment as can be easily checked from its definition. Then (10) implies that the corresponding details vanish when the function u is locally constant.

Higher vanishing moments. In order to realize a better compression by exploiting a higher order smoothness we have to raise the order of vanishing polynomial moments. The basic idea is first to construct the box wavelets $\tilde{\psi}_\lambda^H$, $\lambda \in I_l$, cf. [37, 54], and then to modify the box wavelet by some coarse grid box functions $\tilde{\phi}_\mu$, $\mu \in I_l$, leading to the ansatz

$$\tilde{\psi}_\lambda := \tilde{\psi}_\lambda^H + \sum_{\mu \in L_\lambda} l_\mu^\lambda \, \tilde{\phi}_\mu, \tag{13}$$

with parameters l_μ^λ that are still to be determined. Here the stencil $L_\lambda \subset I_l$ denotes a finite number of cells V_μ in the local neighborhood of the cell V_λ. Then the parameters l_μ^λ are chosen such that (12) holds for all polynomials p of degree less than M. This will lead to a linear system of equations for the coefficients l_μ^λ. In higher dimensions, the cardinality of the stencil L_λ is typically chosen larger than the number of conditions imposed by (12). Then the under-determined system can be solved using the Moore-Penrose inverse.

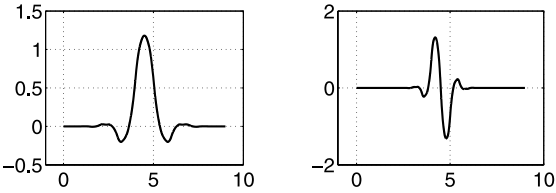

Fig. 3 Primal scaling function $\phi_{0,0}$ (left) and primal wavelet $\psi_{0,0}$ (right) corresponding to the modified Haar wavelet $\tilde{\psi}_{0,0}$ with $s = 2$

Example. Modified Haar wavelets with higher vanishing moments $M = 2s+1$ can be obtained according to the above procedure where we choose $L_{l,k} = \{k - s, \ldots, k+s\}$. In this particular case, the resulting linear system has a unique solution. Furthermore, there exists a primal system of scaling and wavelet functions that is biorthogonal to the dual system of the box function and the modified Haar wavelet. For $s = 2$ the modified Haar wavelet and the corresponding primal functions are shown in Figures 2 (right) and 3, respectively. The biorthogonal system coincides with the system derived from the pair ${}_1\tilde{\Phi}$, ${}_{1,\tilde{N}}\tilde{\Psi}$ and ${}_1\Phi$, ${}_{1,\tilde{N}}\Psi$ corresponding to the B-spline function ${}_1\tilde{\Phi} = \chi_{[0,1]}$ of order 1 with $\tilde{N} = M = 2s+1$ as constructed in [24]. Note that for our purposes the dual and the primal functions are normalized with respect to L^1 and L^∞, respectively, instead of L^2 in [24].

Multiscale Transformation. In order to exploit the above compression potential, the idea is to transform the array of cell averages $u_L := (\hat{u}_\lambda)_{\lambda \in I_L}$ corresponding to a finest uniform discretization level into a sequence of coarse grid data $u_0 := (\hat{u}_\lambda)_{\lambda \in I_0}$

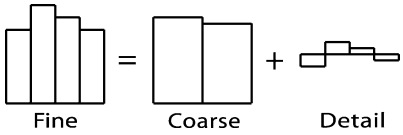

Fig. 4 Two-scale Transformation

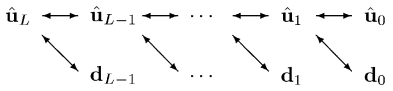

Fig. 5 Multiscale transformation

and details $d_l := (d_\lambda)_{\lambda \in J_l}$, $l = 0, \ldots, L-1$, representing the successive update from a coarser resolution to a higher resolution.

In summary, according to (7) and (10), the change of basis provides two–scale relations for the coefficients inherited from the two–scale relations of the box functions and the wavelet functions

$$\hat{u}_\lambda = \sum_{\mu \in M_\lambda^0 \subset I_{l+1}} m_{\mu,\lambda}^{l,0}\, \hat{u}_\mu, \quad \lambda \in I_l, \qquad d_\lambda = \sum_{\mu \in M_\lambda^1 \subset I_{l+1}} m_{\mu,\lambda}^{l,1}\, \hat{u}_\mu, \quad \lambda \in J_l, \tag{14}$$

and, conversely,

$$\hat{u}_\lambda = \sum_{\mu \in G_\lambda^0 \subset I_l} g_{\mu,\lambda}^{l,0}\, \hat{u}_\mu + \sum_{\mu \in G_\lambda^1 \subset J_l} g_{\mu,\lambda}^{l,1}\, d_\mu, \qquad \lambda \in I_{l+1}, \tag{15}$$

which reflects the typical cascadic format of a wavelet transform. The two-scale relations are illustrated for the 1D case in Figure 4.

A successive application of the relations (14), see Figure 5, decomposes the array $\hat{u}_L$ into coarse scale averages and higher level fluctuations. We refer to this transformation as the *multiscale transformation*. It is inverted by the *inverse multiscale transformation* (15).

4 Multiscale-based spatial grid adaptation

To determine a locally refined grid we employ the above multiscale decomposition. The basic idea is to perform data compression on the vector of detail coefficients using hard thresholding as suggested by the cancellation property. This will significantly reduce the complexity of the data. Based on the thresholded array we then perform local grid adaptation where we refine a cell whenever there exists a significant detail, i.e. a detail coefficient with absolute value above the given threshold. The main steps in this procedure are summarized in the following:

Step 1: Multiscale analysis. Let v_L^n be the cell averages representing the discretized flow field at some fixed time step t^n on a given locally refined grid with highest level of resolution $l = L$. This sequence is encoded in arrays of *detail coefficients* d_l^n, $l = 0, \ldots, L-1$ of ascending resolution, see Figure 5, and cell averages on some coarsest level $l = 0$. For this purpose the multiscale transformation (14) needs to be performed *locally* which is possible due to the locality of the mask coefficients.

Step 2: Thresholding. In order to compress the original data we discard all detail coefficients d_λ whose absolute values fall below a level-dependent threshold value $\varepsilon_l = 2^{l-L}\varepsilon$. Let

$$D^n_{L,\varepsilon} := \left\{\lambda \ ; \ |d^n_\lambda| > \varepsilon_l, \ \lambda \in I_l, \ l \in \{0,\ldots,L-1\}\right\}$$

be the set of *significant details*. The ideal strategy would be to determine the threshold value ε such that the *discretization error* of the reference scheme, i.e., difference between exact solution and reference scheme, and the *perturbation error*, i.e., the difference between the reference scheme and the adaptive scheme, are balanced. For a detailed treatment of this issue we refer to [25].

Step 3: Prediction and grading. Since the flow field evolves in time, grid adaptation is performed after each evolution step to provide the adaptive grid at the *new* time step. In order to guarantee the adaptive scheme to be *reliable* in the sense that no significant future feature of the solution is missed, we have to *predict* all significant details at the new time step $n+1$ by means of the details at the *old* time step n. Let $\tilde{D}^{n+1}_{L,\varepsilon}$ be the prediction set satisfying the *reliability condition*

$$D^n_{L,\varepsilon} \cup D^{n+1}_{L,\varepsilon} \subset \tilde{D}^{n+1}_{L,\varepsilon}. \tag{16}$$

Basically there are two prediction strategies (i.e. ways of choosing $\tilde{D}^{n+1}_{L,\varepsilon}$) discussed in the literature, see [40, 25]. Moreover, in order to perform the grid adaptation process, this set is additionally inflated somewhat such that the grid refinement history, i.e., the parent-child relations of subdivided cells, corresponds to a *graded* tree. Then the set of significant details can be interpreted as a graph where all details are connected by an edge in the graph.

Step 4: Grid adaptation. By means of the set $\tilde{D}^{n+1}_{L,\varepsilon}$ a locally refined grid is determined along the following lines. We check for the transformed flow data represented on $\tilde{D}^{n+1}_{L,\varepsilon}$ proceeding levelwise from coarse to fine whether the detail associated with any cell marked by the prediction set is significant or not. If it is, we refine the respective cell. We finally obtain the locally refined grid with hanging nodes represented by the index set $\tilde{G}^{n+1}_{L,\varepsilon}$. The flow data on the new grid can be computed from the detail coefficients in the same loop where we locally apply the inverse multiscale transformation (15).

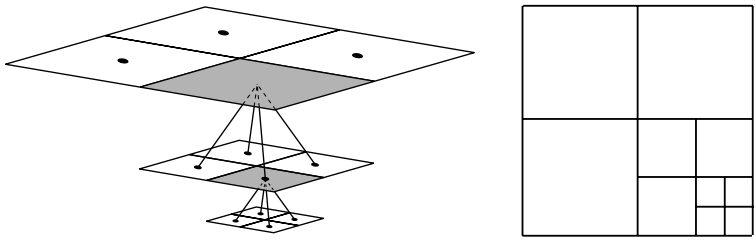

Fig. 6 Grid adaptation: refinement tree (left) and corresponding adaptive grid (right)

5 Adaptive multiresolution finite volume schemes

The rationale behind our design of adaptive multiresolution finite volume schemes (MR-FVS) is to accelerate a given finite volume scheme (reference scheme) on a uniformly refined mesh (reference mesh) by computing actually *only* on a locally refined adapted subgrid, while preserving (up to a fixed constant multiple) the accuracy of the discretization on the full uniform grid. We shall briefly indicate now how to realize this strategy with the aid of the ingredients discussed in the previous section.

5.1 From the reference scheme to an adaptive scheme

The conceptual starting point is to rewrite the evolution equations (2) for the cell averages v_λ, $\lambda \in I_L$, of the reference scheme in terms of evolution equations for the multiscale coefficients. For this purpose we apply the multiscale transformation (14) to the set of evolution equations (2). Then we discard all equations that do not correspond to the prediction set $\tilde{D}^{n+1}_{L,\varepsilon}$ of significant details. Finally we apply locally the inverse multiscale transformation (15) and obtain the evolution equations for the cell averages on the adaptive grid $\tilde{G}^{n+1}_{L,\varepsilon}$ which is obtained from $\tilde{D}^{n+1}_{L,\varepsilon}$ as explained before:

$$v^{n+1}_\lambda = v^n_\lambda - \lambda_\lambda \, (\overline{B}^n_\lambda + |V_\lambda| \overline{S}^n_\lambda), \tag{17}$$

for all $\lambda \in \tilde{G}^{n+1}_{L,\varepsilon}$ where $\lambda_\lambda := \Delta t^{n+1}/|V_\lambda|$. Here the flux balances $\overline{B}^n_\lambda$, the numerical fluxes $\overline{F}^n_\lambda$ and the source terms $\overline{S}^n_\lambda$ are recursively defined from fine to coarse scale via

$$\overline{B}^n_\lambda = \sum_{\Gamma^l_{\lambda,\mu} \subset \partial V_\lambda} |\Gamma^l_{\lambda,\mu}| \overline{F}^{l,n}_{\lambda,\mu}, \tag{18}$$

$$\overline{F}^{l,n}_{\lambda,\mu} = \sum_{\Gamma^{l+1}_{\mu,\nu} \subset \Gamma^l_{\lambda,\mu}} |\Gamma^{l+1}_{\mu,\nu}| \overline{F}^{l+1,n}_{\mu,\nu} = \ldots = \sum_{\Gamma^L_{\mu,\nu} \subset \Gamma^l_{\lambda,\mu}} |\Gamma^L_{\mu,\nu}| F(v^n_{L,\mu\nu}, v^n_{L,\nu\mu}, \mathbf{n}_{L,\mu\nu}), \tag{19}$$

$$\overline{S}^n_\lambda = \sum_{V_\mu \subset V_\lambda, \mu \in I_{l+1}} \frac{|V_\mu|}{|V_\lambda|} \overline{S}^n_\mu = \ldots = \sum_{V_\mu \subset V_\lambda, \mu \in I_L} \frac{|V_\mu|}{|V_\lambda|} S(v^n_\mu). \tag{20}$$

We refer to (19) and (20) as *exact flux and source reconstruction*, respectively. Since in (20) we have to compute *all* sources on the finest scale, there is no complexity reduction, i.e., we still have the complexity $\#I_L$ of the reference mesh. In order to gain efficiency we therefore have to replace the exact flux and source reconstruction by some approximation such that the overall accuracy is maintained. The local flux and source computation and the choice of the prediction set $\tilde{D}^{n+1}_{L,\varepsilon}$ will be discussed in detail in Section 5.2 and 5.3, respectively.

The complete adaptive scheme consists now of the following three steps:

Step 1. (*Refinement*) Determine the prediction set $\tilde{D}^{n+1}_{L,\varepsilon}$ from the data of the old

time step t^n and project the data of the old time step onto the pre-refined grid $\tilde{G}_{L,\varepsilon}^{n+1}$ of the new time step, i.e.,

$$\{v_\lambda^n\}_{\lambda\in G^n} \to \{v_\lambda^n\}_{\lambda\in\tilde{G}^{n+1}}.$$

Step 2. (*Evolution*) Evolve the cell averages associated to the pre-refined grid $\tilde{G}_{L,\varepsilon}^{n+1}$ according to (17), where the numerical fluxes and sources are not necessarily determined by (19) and (20), respectively, i.e.,

$$\{v_\lambda^n\}_{\lambda\in\tilde{G}_{L,\varepsilon}^{n+1}} \to \{v_\lambda^{n+1}\}_{\lambda\in\tilde{G}_{L,\varepsilon}^{n+1}}.$$

Step 3. (*Coarsening*) Compress the data of the new time step by thresholding the corresponding detail coefficients and project the data to the (somewhat coarsened new) adaptive grid $G_{L,\varepsilon}^{n+1}$, i.e.,

$$\{v_\lambda^{n+1}\}_{\lambda\in\tilde{G}_{L,\varepsilon}^{n+1}} \to \{v_\lambda^{n+1}\}_{\lambda\in G_{L,\varepsilon}^{n+1}}.$$

5.2 Approximate flux and source approximation strategies

As already mentioned above, the adaptive MR-FVS with exact flux and source reconstruction (19) and (20) will have the same complexity as the reference scheme performed on the reference mesh. If there is no inhomogeneity, i.e., $s \equiv 0$, then the complexity of the resulting algorithm might be significantly reduced from the cardinality of the reference mesh to the cardinality of the refined mesh. To see this we note that, due to the nestedness of the grid hierarchy and the conservation property of the numerical fluxes, the coarse-scale flux balances are only computed by the fine-scale fluxes corresponding to the edges of the coarse cells, see (19). Those in turn, have to be determined by the fine scale data. However, the internal fluxes are canceled and, hence, the overall complexity is reduced. For instance, for a d-dimensional Cartesian grid hierarchy we would have to compute $2d\,2^{(L-l)(d-1)}$ fluxes corresponding to all fine-scale interfaces $\mu \in I_L$ with $\partial V_\mu \subset \partial V_\lambda$ where $\lambda \in I_l$, $l \le L$, due to the subdivision of the cell faces. Note that in both cases missing data on the finest scale have to be determined by locally applying the inverse two-scale transformation. This is illustrated in Figure 7. On the other hand, the coarse scale sources can be computed similarly with the aid of the recursive formulae (20). Here, however, we have to compute *all* sources on the finest scale which at the first glance prevents the desired complexity reduction.

Hence the adaptive scheme with both exact flux and source reconstruction is useless for practical purposes. However, in the reliability analysis one may perform the adaptive scheme with some approximate flux and source reconstruction to be considered as a further perturbation of the "exact" adaptive scheme.

Fig. 7 Exact (left) versus local (right) flux and source computation

In order to retain efficiency we therefore have to replace the exact flux and source reconstruction by some approximation such that the overall accuracy is maintained. A naive approach would be to use the local data provided by the adaptive grid, i.e.,

$$\overline{F}^{l,n}_{\lambda,\mu} = F(v^n_{l,\lambda\mu}, v^n_{l,\mu\lambda}, \mathbf{n}_{l,\lambda\mu}), \quad \overline{S}^n_\lambda = S(v^n_\lambda) \tag{21}$$

for $\lambda, \mu \in I_l$.

So far, this approach is applied in Quadflow. Obviously, the complexity of the resulting adaptive MR-FVS is reduced to the cardinality of the adaptive grid. Unfortunately, this approach may suffer from serious loss in accuracy in comparison with the reference scheme.

Recently, in [44] a new approach was suggested using an approximate flux and source reconstruction strategy that are discussed along the following lines:

Step 1. Determine for each cell V_λ, $\lambda \in \tilde{G}^{n+1}_{L,\varepsilon}$, a higher order reconstruction polynomial R^N_λ of degree N using only local data corresponding to the adaptive grid.
Step 2. Approximate the boundary and volume integrals in (19) and (20) by some appropriate quadrature rules.
Step 3. Compute fluxes and source terms in quadrature nodes by determining point-values or cell averages on level L of the local reconstruction polynomial R^N_λ, respectively.

This concept has been analyzed in detail for the 1D case, cf. [44]. In particular, it was proven that the accuracy of the reference scheme can be maintained when using the prediction strategy in [25] and appropriately tuning the parameters such as the reconstruction order and the quadrature rules. Computations verify the analytical results. Therefore the new approach seems to be superior to the naive approach with respect to accuracy and efficiency.

5.3 Prediction strategies

The accuracy of the adaptive scheme crucially relies on the grid refinement process. In our case it is triggered by the details. In order to guarantee that all significant flow features are always adequately resolved, we have to pre-refine the grid before performing the time evolution. For this purpose, we have to *predict* all details $\tilde{D}_{L,\varepsilon}^{n+1}$ on the *new* time step that may become significant due to the evolution by means of the details $D_{L,\varepsilon}^{n}$ on the *old* time step. We consider the prediction set $\tilde{D}_{L,\varepsilon}^{n+1}$ to be reliable, if the reliability condition (16) is satisfied in each time step where, of course, $D_{L,\varepsilon}^{n+1}$ is not known yet. Then no significant future feature of the solution is missed on the old and the new time step, respectively.

Harten's strategy. A first strategy was proposed by Harten in [40]. The basic idea of his heuristic approach is based on two characteristic features of hyperbolic conservation laws: (i) details in a local neighborhood $N_\lambda^q := \{\mu \in I_l\,;\, \|\mu - \lambda\|_\infty \le q\}$ of a significant detail $\lambda \in I_l$ may also become significant within one time step, i.e.,

$$\lambda \in D_{L,\varepsilon}^{n} \quad \Rightarrow \quad \tilde{D}_{L,\varepsilon}^{n+1} = \tilde{D}_{L,\varepsilon}^{n+1} \cup N_\lambda^q, \tag{22}$$

due to the finite speed of propagation, and (ii) gradients may become steeper causing significant details on a higher refinement level due to the developing of discontinuities, i.e.,

$$\lambda \in D_{L,\varepsilon}^{n} \quad \Rightarrow \quad \tilde{D}_{L,\varepsilon}^{n+1} = \tilde{D}_{L,\varepsilon}^{n+1} \cup M_\lambda^0, \tag{23}$$

where $M_\lambda^0 \subset I_{l+1}$ is the refinement set of cell V_λ, $\lambda \in I_l$. Note that the choice of q in (22) depends on the CFL number. If the CFL number is less than 1, that is reasonable for explicit time discretizations, we may choose $q = 1$. However, in case of an implicit time discretization higher CFL numbers might be admissible. In this case an information could move by more than one cell and we have to adjust q accordingly. In general, the range of influence of an information within one time step depends on the configuration at hand. If the flow field is weakly instationary, cf. [69], or even stationary, cf. [15], then an information will not move by as many cells as is indicated by the CFL number, cf. [27]. This also holds in case of small parabolic perturbations due to viscosity terms, cf. [11].

So far Harten's approach could not be rigorously verified to satisfy (16). Nevertheless, it is frequently used in applications and turned out to give good results.

Strategy by Cohen et al.. A slight modification of Harten's prediction strategy has been shown to lead to a reliable prediction strategy in the sense of (16). This was rigorously proven for a certain class of *explicit* finite volume schemes applied to *one–dimensional scalar* conservation laws *without source terms* on *uniform dyadic grids* as base hierarchies, using exact flux reconstruction, cf. [25]. Recently, the proof has been extended for conservation laws *with* source term using approximate flux and source reconstruction, cf. [44]. In the following we briefly summarize the strategy. For simplicity of representation, we first introduce the convention $d_\lambda := v_\lambda$ for $\lambda \in I_{-1}$, where we identify I_{-1} with I_0 but replace the level $l = 0$ by $l = -1$. Then the prediction set can be determined in three steps:

Step 1: First of all, we determine the influence set D_λ that contains all coefficients d_μ^{n+1} on the new time step which are influenced by a coefficient d_λ^n on the old time step. For this purpose, we first have to compute the *range of influence* Σ_λ of the coefficient d_λ^n and the *domain of dependence* $\tilde{\Sigma}_\mu$ of the coefficient d_μ^{n+1}. In the range of influence we collect the indices of all averages v_ν^n, $\nu \in I_L$, that are influenced by the detail d_λ^n whereas the domain of dependence contains the indices of all averages v_ν^{n+1}, $\nu \in I_L$, that are needed to compute the coefficient d_μ^{n+1}. Note that the index sets $\tilde{\Sigma}_\mu \subset I_L$ and $\Sigma_\lambda \subset I_L$ correspond to data on the reference mesh but for different time steps, $n+1$ and n, respectively. By the evolution process (17) with exact reconstruction (19) and (20), the domain of dependence has to be extended taking into account the stencil $S_\lambda \subset I_l$ of the numerical flux F and source S associated to the cell $\lambda \in I_l$, i.e., $\tilde{\Sigma}_\mu^- := \bigcup_{\lambda \in \tilde{\Sigma}_\mu} S_\lambda$. Then the influence set is determined by

$$D_\lambda = \{\mu \,;\, \tilde{\Sigma}_\mu^- \cap \Sigma_\lambda \neq \emptyset\}.$$

Step 2: The prediction strategy has to take into account that the coefficients d_λ^n may not only cause a perturbation in the neighborhood of the cell V_λ, $\lambda \in I_l$, because of the time evolution but may also influence coefficients d_μ^{n+1}, $\mu \in I_{l'}$, on higher scales, i.e., $l' \geq l+1$. Since the additional higher levels inflate the influence set, we would like to bound the number of higher levels to a minimum number. For this purpose, we fix some $\sigma > 1$ and assign to each coefficient corresponding to $\lambda \in D^n$ a unique index $\nu = \nu(\lambda)$ such that

$$\begin{aligned} 2^{\nu(\lambda)\sigma}\varepsilon_l < |d_\lambda^n| \leq 2^{(\nu(\lambda)+1)\sigma}\varepsilon_l, \quad \lambda \in I_l,\ l \in \{0,\dots,L-1\},\\ 2^{\nu(\lambda)\sigma}\varepsilon_0 < |v_\lambda^n| \leq 2^{(\nu(\lambda)+1)\sigma}\varepsilon_0, \quad \lambda \in I_0. \end{aligned}$$

This process is referred to as *nesting of details*. The parameter σ is linked to the smoothness of the primal wavelet functions, cf. [25]. Since the index $\nu(\lambda)$ becomes smaller the larger σ is, it is convenient to choose σ as large as possible.

Step 3: Finally, we determine the prediction set from the influence set D_λ and the nesting of coefficients

$$\tilde{D}_{L,\varepsilon}^{n+1} := D_{L,\varepsilon}^n \cup \bigcup_{\lambda \in D_{L,\varepsilon}^n \cup I_{-1}} \{\mu \,;\, \mu \in D_\lambda \setminus I_{-1} \text{ and } l' \leq l + \nu(\lambda)\}. \tag{24}$$

Note that opposite to Harten's original prediction strategy, a significant detail might affect cells not only at one higher level but up to $\nu(\lambda)$ additional scales.

5.4 Multilevel time stepping

For instationary problems, the time step is typically restricted for stability reasons by some CFL condition. This holds true even for implicit time discretizations due to nonlinear stability criteria, e.g., total variation diminishing (TVD) property. There-

fore the time stepsize has to be bounded by the smallest cell in the grid. Hence τ is determined by the CFL condition on the highest refinement level L, i.e., $\tau = \tau_L$. For reasons of simplicity, we neglect the time index n here. However, for cells on the coarser scales $l = 0, \ldots, L-1$ we may use $\tau_l = 2^{L-l}\,\tau_L$ to locally satisfy the CFL condition.

In [56] a local time stepping strategy has been incorporated into the adaptive multiresolution finite volume scheme as presented in previous sections. This strategy has been extended to multidimensional problems in [53, 52]. Here ideas similar to the predictor-corrector scheme [58] and the adaptive mesh refinement (AMR) technique [10, 9] are used. The differences between classical approaches and the multilevel strategy are discussed in [56] in detail.

Time evolution. The basic idea is to evolve each cell on level l with the level-dependent time discretization $\tau_l = 2^{L-l}\,\tau_L$, $l = 0, \ldots, L$. Obviously, after having performed 2^l time steps with τ_l, all cell averages correspond to the same integration time, i.e., the cells are *synchronized*. Therefore one macro time step with $\tau_0 = 2^L\,\tau_L$ consists of 2^L intermediate time steps with step size τ_L. Obviously, at time $t_{n+i2^{-L}}$ all cells on levels $l = l_i, \ldots, L$ are synchronized. Here l_i denotes the *smallest synchronization level* that is determined by

$$l_i := \min\{l;\, 0 \le l \le L,\ i \bmod 2^{L-l} = 0\}, \quad i = 0, \ldots, 2^L - 1.$$

Then the time evolution for the intermediate time steps $i = 0, \ldots, 2^L - 1$, takes the form

$$v_\lambda^{n+(i+1)2^{-L}} = v_\lambda^{n+i2^{-L}} - \lambda_\lambda\,(\overline{B}_\lambda^{n+i2^{-L}} + |V_\lambda|\,\overline{S}_\lambda^{n+i2^{-L}}), \tag{25}$$

for any cell $\lambda \in \tilde{G}_{L,\varepsilon}$ of the current locally adapted grid. Similar to (18) the numerical flux balance is determined by

$$\mathbf{B}_\lambda^{n+i2^{-L}} = \sum_{\Gamma_{\lambda,\mu}^l \subset \partial V_\lambda} |\Gamma_{\lambda,\mu}^l|\,\overline{F}_{\lambda,\mu}^{l,n+i2^{-L}}.$$

However, the numerical flux computation is performed differently. Here the basic idea is (i) to update the fluxes on the synchronized levels $l_i \le l \le L$, whereas (ii) for all other interfaces we do not update the numerical flux but use the same value as in the previous intermediate time step. In detail, we proceed as follows: (i) if the neighbor cell V_μ is living on the same level l, then we apply the flux computation strategy as in case of global time stepping, where we either use the exact strategy (19), the naive strategy (21), or the reconstruction strategy according to Section 5.2, respectively. Alternatively, the neighboring cell could live on the finer level $l+1$ due to grid refinement. Then there exist hanging nodes at the interface $\Gamma_{\lambda,\mu}^l$. and we compute the numerical flux by the fluxes on the finer scale, i.e.,

$$\overline{F}_{\lambda,\mu}^{l,n+i2^{-L}} = \sum_{\Gamma_{\mu,\nu}^{l+1} \subset \Gamma_{\lambda,\mu}^l} |\Gamma_{\mu,\nu}^{l+1}|\,\overline{F}_{\mu,\nu}^{l+1,n+i2^{-L}}. \tag{26}$$

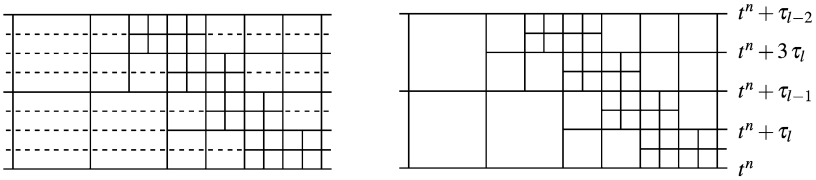

Fig. 8 Synchronized time evolution on space-time grid, horizontal axis: 1D space, vertical axis: time

This is motivated by (19) and immediately implies the conservation property of the scheme. Note that the refinement level of two adjacent cells differs by at most one, i.e., there is at most one hanging node at one edge. This can be ensured by a grading process of the adaptive grid, cf. Section 4. (ii) For all other interfaces in the adaptive grid we use the flux of the previous intermediate time step, i.e.,

$$\overline{F}_{\lambda,\mu}^{l,n+i2^{-L}} = |\Gamma_{\mu,\nu}^{l}|\,\mathbf{F}_{\lambda}^{n+(i-1)2^{-L}}. \tag{27}$$

To ensure that the fluxes at an interface with hanging nodes have already been computed when determining the corresponding flux on the coarser level, we perform in each intermediate time step the time evolution first for the cells on the highest level and then successively for the coarser levels. This procedure is similar to the predictor-corrector method in [58].

The source terms are updated accordingly, where we either apply the naive strategy (21) or the reconstruction strategy, cf. Section 5.2, respectively, on the synchronized levels $l_i \le l \le L$ or use the source term from the previous intermediate time step for the non-synchronized levels $l < l_i$, i.e.,

$$\mathbf{S}_{\lambda}^{n+i2^{-L}} = \mathbf{S}_{\lambda}^{n+(i-1)2^{-L}}. \tag{28}$$

Note that for the lower levels $0,\dots,l_i-1$ we do not compute new fluxes or source terms. This makes the local time stepping version of the adaptive multiresolution concept more efficient then the standard approach using a global time stepsize. However, book-keeping of the interfaces with hanging nodes is time consuming and the algorithms become hard to read and to implement, cf. [56, 27]. In practice, it is more convenient to perform the time evolution (25) for *all* cells of the adaptive grid for *all* intermediate time steps. Then all data are synchronized at any time. Of course, there is a small overhead to perform (25) for non-synchronized level $l < l_i$. However, this is negligible in comparison to the time needed to evaluate the original numerical fluxes that typically requires the solution of some Riemann problem. Then only few changes are needed to embed the multilevel time stepping into an existing code.

In Figure 8 the time evolution algorithm is schematically illustrated in the one-dimensional case: In a global time stepping, i.e., using $\Delta t = \tau_L$ for all cells, each vertical line section appearing in Fig. 8 (left) represents a flux evaluation and each horizontal line (dashed or solid) represents a cell update of the cell average due to

the fluxes. In the multilevel time stepping a flux evaluation is only performed at vertical line sections that emanate from a point where at least one solid horizontal line section is attached. If a vertical line section emanates from a point, where two dashed horizontal sections are attached, then we do not recompute the flux, but keep the flux value from the preceeding vertical line section. Hence fluxes are only computed for the vertical edges in Fig. 8 (right).

Intermediate grid adaptation. Finally, we have to comment on the grid adaptation step. The ultimate goal is to provide an approximation after one macro time step with $\tau_0 = 2^L \tau_L$ as good as having performed 2^L time steps with the reference scheme on the reference mesh using the time step size τ_L. Therefore we have to make sure that the solution is adequately resolved at each intermediate time step.

For the original adaptive multiresolution scheme this is ensured by the prediction step of the grid adaption, see Section 5.3. The prediction of the details ensures that a significant information can only move by at most one cell on the *finest* level, e.g. controlled by parameter q in (22) typically set to 1. However, by employing the same strategy for the local time stepping this information could move up to one cell on the *coarsest* mesh or 2^L cells on the *finest* mesh, respectively. This would result in a completely underresolution of discontinuities on the new time step. To account for this we have to modify the prediction set $\tilde{D}_{L,\varepsilon}^{n+1}$ such that the modified reliability condition

$$\bigcup_{i=0}^{2^L} D_{L,\varepsilon}^{n+i2^{-L}} \subset \tilde{D}_{L,\varepsilon}^{n+1}, \tag{29}$$

holds where the sets $D_{L,\varepsilon}^{n+i2^{-L}}$ correspond to the significant details of the solution at the intermediate times $t_{n+i2^{-L}} = t_n + i\,\tau_L$, $i = 0, \ldots, 2^L$.

Obviously, using $q = 2^L$ would ensure that all effects are properly resolved on the new time step after having performed the macro time step. However, the efficiency degrades tremendously. A very efficient and reliable alternative was suggested in [56]. The idea is to perform additional grid adaptation steps according to Section 4 before each even intermediate time step, i.e., $i = 0, 2, \ldots, 2^L - 2$. However, we do not apply the adaptation process for the whole computational domain, but only for the cells on the levels $l = l_i, \ldots, L$, i.e., level l_i is considered to be the coarsest scale in the multiscale analysis. Note, that only for this range of scales new fluxes and sources have to be recomputed. This process provides us with the sets $G_{L,\varepsilon}^{n+(i+1)2^{-L}}$ for which we perform the evolution step (25). For the odd intermediate time steps we use the same grid as in the previous step, i.e., $G_{L,\varepsilon}^{n+i2^{-L}} = G_{L,\varepsilon}^{n+(i-1)2^{-L}}$, $i = 1, 3, \ldots, 2^L - 1$. Hence, it is possible to track, for instance, the shock position on the intermediate time steps instead of a-priori refining the whole range of influence, see Fig. 8 (right).

5.5 Error analysis

The performance of the adaptive MR-FVS crucially depends on the threshold parameter ε. With decreasing value the adaptive grid becomes richer and, finally, if ε tends to zero, we obtain the uniform reference mesh, i.e., the adaptive scheme coincides with the reference scheme. On the other hand, the adaptive grid becomes coarser with increasing threshold value, i.e., the computation becomes faster but provides a less accurate solution. An ideal choice would maintain the accuracy of the reference scheme at reduced computational cost. For a detailed analysis we refer to [25, 44] and explain only the main ideas here.

In order to estimate the error, we introduce the averages $\hat{u}_L^n$ of the exact solution, the averages v_L^n determined by the reference FVS and the averages $\overline{v}_L^n$ of the adaptive scheme prolongated to the reference mesh by means of the inverse multiscale transformation where non-significant details are simply set to zero. Ideally one would like to choose the threshold ε so as to guarantee that $\|\hat{u}_L^n - \overline{v}_L^n\| \leq tol$ where tol is a given target accuracy and $\|\cdot\|$ denotes the standard weighted l^1-norm. Since $\overline{v}_L^n$ can be regarded as a perturbation of v_L^n, this is only possible if L is chosen so as to ensure that the reference scheme is sufficiently accurate, i.e. one also has $\|\hat{u}_L^n - v_L^n\| \leq tol$. Again ideally, a possibly low number of refinement levels L should be determined during the computation such that the error meets the desired tolerance $\|\hat{u}_L^n - \overline{v}_L^n\| \leq tol$. Since no explicit error estimator is available for the adaptive scheme, we try to assess the error by splitting the error into two parts corresponding to the *discretization error* $\tau_L^n := \hat{u}_L^n - v_L^n$ of the reference FVS and the *perturbation error* $e_L^n := v_L^n - \overline{v}_L^n$. We now assume that there is an a priori error estimate of the discretization error, i.e., $\tau_L^n \sim h_L^\alpha$ where h_L denotes the spatial step size and α the convergence order. Then, ideally we would determine the number of refinement levels L such that $h_L^\alpha \sim tol$. In order to preserve the accuracy of the reference FVS, we may now admit a perturbation error which is proportional to the discretization error, i.e., $\|e_L^n\| \sim \|\tau_L^n\|$. From this, one can derive a suitable level $L = L(tol, \alpha)$ and $\varepsilon = \varepsilon(L)$.

Therefore it remains to verify that the perturbation error can be controlled. To this end, note that in each time step we introduce an error due to the thresholding procedure. Obviously, this error accumulates in each step, i.e., the best we can hope for is an estimate of the form $\|e_L^n\| \leq C n \varepsilon$. However, the threshold error may be amplified in addition by the evolution step. In order to control the cumulative perturbation error, we have to prove that the constant C is independent of L, n, τ and ε. For a simplified model problem this was rigorously done in [25] for homogeneous problems and exact reconstruction and, recently, in [44] for inhomogeneous problems using approximate flux and source reconstruction.

6 Numerical results

Finally, we would like to demonstrate that the multiscale-based grid adaptation concept has been developed beyond pure academic investigations and can be applied

to real-world problems. For this purpose, we present the results of 3D simulations that have been recently performed with the new solver Quadflow for a challenging problem arising in aerodynamics.

6.1 The solver Quadflow

The above multiscale-based grid adaptation concept has been integrated into the new adaptive and parallel solver Quadflow [14, 15]. This solver has been developed for more than one decade within the collaborative research center SFB 401 *Modulation of Flow and Fluid-Structure Interaction at Airplane Wings*, cf. [3, 65]. In order to exploit synergy effects, it has been designed as an *integrated* tool where each of the core ingredients, namely, (i) the flow solver concept based on a finite volume discretization [13], (ii) the grid adaptation concept based on wavelet techniques [54], and (iii) the grid generator based on B-spline mappings [51] is adapted to the needs of the others. In particular, the three tools are not just treated as independent black boxes communicating via interfaces. Instead, they are highly intertwined on a conceptual level mainly linking (i) the multiresolution-based grid adaption that reliably detects and resolves all physical relevant effects, and (ii) the B-spline grid generator which reduces grid changes to just moving a few control points whose number is, in particular, independent of any local grid refinement. The mathematical concepts have been complemented recently by parallelization techniques that are indispensable for further reducing the computational time to an affordable order of magnitude when dealing with realistic 3D computations for complex geometries, cf. [18, 4].

6.2 Application

The efficiency of an airport is strongly influenced by the takeoff and landing frequency that is determined by the system of vortices generated at the wing tips. These vortices continue to exist for a long period of time in the wake of an airplane, see Figure 9. It is possible to detect wake vortices as far as 100 wing spans behind the airplane, which are a hazard to following airplanes. In the SFB 401, the research aimed to induce instabilities into the system of vortices to accelerate their collapse. The effects of different measures, e.g. additional flaps installed at each airfoil, taken in order to destabilize the vortices have been examined in a water tunnel. A model of a wing was mounted in a water tunnel and the velocity components in the area behind the wing were measured using particle image velocimetry It was possible to conduct measurements over a length of 4 wing spans. The experimental analysis of a system of vortices far behind the wing poses great difficulties due to the size of the measuring system. Numerical simulations are not subject to such severe constraints and therefore Quadflow is used to examine the behavior of vortices far behind the wing. To minimize the computational effort, the grid adaptation adjusts the refine-

ment of the grid with the goal to resolve all important flow phenomena, while using as few cells as possible.

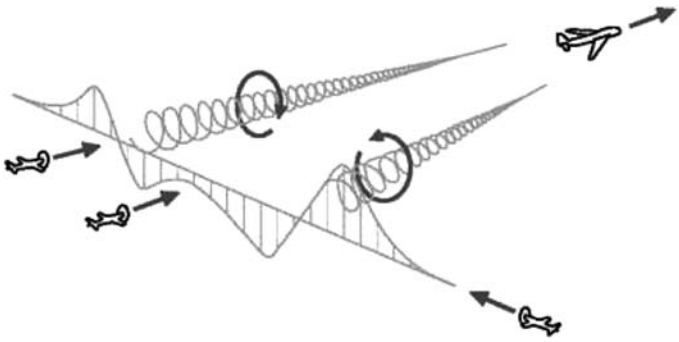

Fig. 9 System of wing tip vortices in the wake of an airplane. (Courtesy of Institute of Aeronautics and Astronautics, RWTH Aachen)

In the present study instationary, quasi incompressible, inviscid fluid flow described by the Euler equations is considered. An assessment is presented to validate the ability of Quadflow to simulate the behavior of the wake of an airplane. A velocity field based on the experimental measurements is prescribed as boundary condition in the inflow plane. Here the measured velocity fields at the wing tip and at the flap, respectively, have been used to generate two different Lamb-Oseen vortices. These vortices are used to specify the circumferential part of the velocity distribution $v_\Theta(r)$. The circumferential velocity distribution of one Lamb-Oseen vortex is computed by

$$v_\Theta(r) = \frac{\Gamma}{2\pi r}\left(1 - e^{-\left(\frac{r}{d_0}\right)^2}\right). \tag{30}$$

The radius r is the distance from the center of a boundary face in the inflow plane to the vortex core. The two parameters of the Lamb-Oseen vortices, circulation Γ and core radius d_0 are chosen in such a way that the models fit to the measured velocity field of the wing tip vortex and the flap vortex as close as possible, respectively. As observed in the experiment, both vortices are rotating in the same direction. The circumferential part of the velocity distribution at the inflow boundary is computed by the superposition of the velocity distribution of both vortices. The axial velocity component in the inflow direction is set to the constant inflow velocity of the water tunnel.

Instead of water, which is used as fluid in the experiment to visualize the vortices, the computation relies on air as fluid. This is justified because of the low Mach number $Ma = 0.05$ and, hence, compressibility effects are negligible. The inflow velocity in the x-direction, u_∞, is computed to fulfill the condition that the Reynolds number in the computational test case is the same as in the experiment.

The experimental conditions are a flow velocity $u_w = 1.1\,\mathrm{m\,s^{-1}}$ and a Reynolds number $Re_w = 1.9 \times 10^5$. From the condition $Re_{air} = Re_w$ the inflow velocity in the x-direction has been determined as $u_\infty = 16.21\,\mathrm{m\,s^{-1}}$. For purpose of consistency, the circumferential velocity v_θ has also been multiplied by the factor u_∞/u_w. The velocity of the initial solution is set to parallel, uniform flow $u_0 = u_\infty$, $v_0 = w_0 = 0.0$.

The computation[1] has been performed on 32 Intel Xeon E5450 processors running at 3 GHz clock speed. The CPU time spent was about 214 hours. The computational domain matches the experimental setup which extents $l = 6\,\mathrm{m}$ in the x-direction, $b = 1.5\,\mathrm{m}$ in the y-direction and $h = 1.1\,\mathrm{m}$ in the z-direction. The boundaries parallel to the x-direction have been modeled as symmetry walls. This domain is discretized by a coarse grid with 40 cells in flow direction, 14 cells in y-direction and 10 cells in the z-direction. The maximum number of refinement levels has been set to $L = 6$. With this setting, both vortices can be resolved on the finest level by about 80 points in the y-z-plane.

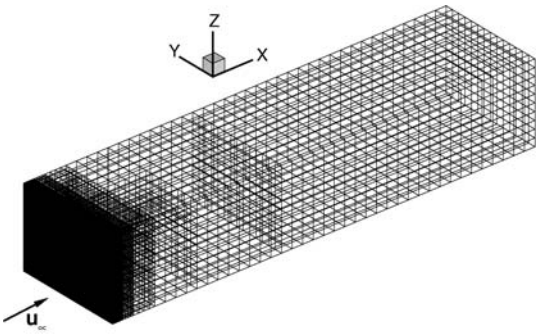

Fig. 10 Initial computational grid

Since Quadflow solves the compressible Euler equations, a preconditioner for low Mach numbers was applied in a dual-time framework acting only on the dual time-derivatives. It has been used for the purposes of numerical discretization and iterative solution, cf. [59]. The spatial discretization of the convective fluxes is based on the AUSMDV(P) flux vector splitting method [32]. For time integration the implicit midpoint rule is applied. In each time step the unsteady residual of the Newton iterations is reduced by about three orders of magnitude. The physical time step is uniformly set to $\Delta t = 5 \times 10^{-5}\,s$ which corresponds to a maximum CFL number of about $CFL_{max} = 28.0$ in the domain. Grid adaptation is performed after each time step. After every 100th time step the load balancing is repeated.

[1] The computations have been performed by Gero Schieffer. They have been made possible by the parallelization concept of space-filling curves embedded in the multiscale library by Silvia-Sorana Mogosan and Kolja Brix.

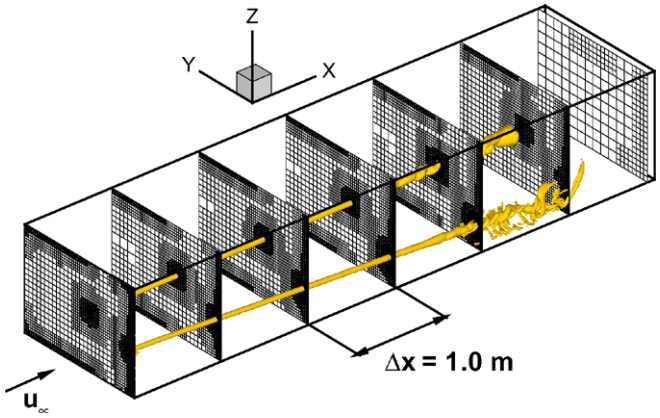

Fig. 11 Slices of the computational grid after 6046 time steps at seven different positions and the distribution of $\lambda_2 = -100$

When the computation starts, the vortices have to be resolved properly on a sufficiently refined grid. For this purpose, the grid on the inflow plane is pre-refined to the maximum level, see Figure 10. Due to this procedure the first grid contains 384000 cells. When the information at the inlet has crossed the first cell layer, the pre-adaptation of the cells at the inlet is no longer needed and then the grid is only adapted according to the adaptation criterion based on the multiscale analysis. For the multiscale analysis we use modified box wavelets with $M = 2$ vanishing moments, see Section 3. The threshold value is set to $\varepsilon = 2.5 \times 10^{-4}$. For the prediction step we apply Harten's original strategy summarized in Section 5.3.

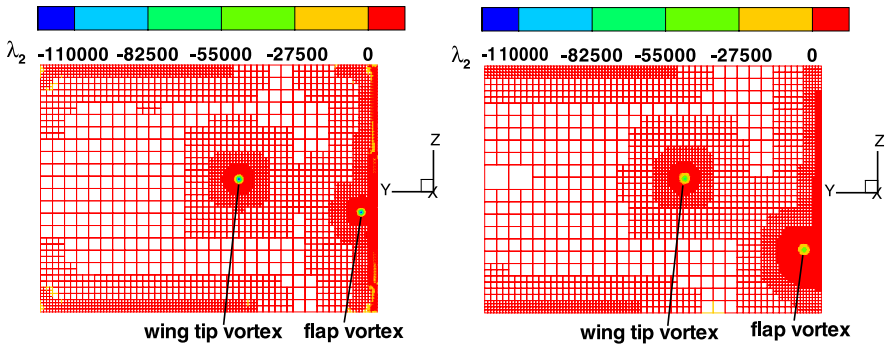

Fig. 12 Slices of the computational grid at two different positions in x-direction, the grid color is consistent with the value of λ_2. Left Figure: Slice of the computational grid at $x = 0.0$ m. Right Figure: Slice of the computational grid at $x = 3.0$ m

After 6046 time steps, which corresponds to a computed real time of $t = 0.3023\,\mathrm{s}$, the grid contains 3.04×10^6 cells in total. This is about 0.2 % of the uniformly refined reference mesh, i.e., by grid adaptation the computational complexity is reduced by a factor of about 500. Figure 11 shows seven cross sections of the mesh, which are equally spaced in x-direction with distances $\Delta x = 1.0\,\mathrm{m}$. In addition, the isosurface of the λ_2-criterion is presented with the value $\lambda_2 = -100$. The λ_2-criterion has been proposed by Jeong et al. [45] to detect vortices. A negative value of λ_2 identifies a vortex, whereas the smallest of these negative values marks the core of the vortex. As can be seen from Figure 11, the vortices are transported through the computational domain. The locally adapted grid exhibits high levels of refinement only in the vicinity of the vortices. A more detailed view of the grid for the cross sections at $x = 0.0\,\mathrm{m}$ and $x = 3.0\,\mathrm{m}$ is presented in Figure 12.

From the engineering point of view, the interaction of the two vortices is of special interest. The central question is whether the strong wing tip vortex can be destabilized by the flap vortex. For this purpose, the computation has to be continued. This is subject of current research. Nevertheless, the computations performed so far verify that the presented concepts are sustainable and necessary in order to investigate this challenging problem.

7 Conclusion and trends

Adaptive multiresolution schemes have turned out be very efficient in numerous applications. In particular, the adaptation process is only controlled by the threshold parameter. The choice of this parameter seems to be very robust with respect to varying configurations and applications. Ideally, it depends on the discretization error of the reference finite volume scheme. This was confirmed by rigorous mathematical estimates for scalar model problems.

Originally, the multiresolution-based grid adaptation technique was kept separate from the treatment of discrete evolution equations. However, the multiresolution analysis offers a much higher potential when applying it directly to the (discrete) evolution equations. Therefore we would like to conclude with some comments on the future development of adaptive multiresolution schemes that is beyond mere grid adaptation.

Trend 1: Adaptive mesh refinement and multiresolution analysis. In order to optimize computational resources, AMR techniques have become a standard way to optimize computational resources. These techniques have been originally developed in the 1980's by Berger et al. [10, 8, 7]. Typically, the refinement process is triggered by gradients [60] or higher order interpolation [2]. Recent investigations by [31] show that using a discrete multiresolution analysis instead leads to a much more efficient refinement criteria. In particular, in areas of partial smoothness such as rarefaction waves. It turned out that only minimal changes in the existing AMR code were necessary to embed the multiresolution-based refinement criterion.

In principle, it would be possible to embed the multiresolution-based grid adaptation concept to any AMR code as a black box, where the data have to be transferred between the two tools. This has been realized in the Quadflow solver [14, 15]. However, this requires some computational overhead in terms of memory and CPU time. In particular, the multiresolution-based grid adaptation technique is kept separate from the treatment of discrete evolution equations and therefore we could not employ the much higher potential of the multiresolution analysis when applying it directly to the discrete evolution.

Trend 2: Implicit time discretization. In Section 5, adaptive multiresolution finite volume schemes have been derived only for explicit time discretizations. We may proceed similarly in case of an implicit time discretization, cf. [15]. These are of interest when dealing with stationary flow problems, weakly instationary problems or models that exhibit some stiffness due to relaxation processes, e.g. chemical reactions, or dissipation, e.g. diffusion, viscosity and heat conduction, resulting in anisotropic flow structures such as boundary layers. For these types of problems an explicit time discretization would lead to very small time steps in order to meet the CFL condition. Although the derivation is straight-forward, several new questions arise:

(i) In each time step the implicit time discretization results in a nonlinear system of discrete evolution equations. Typically this system is solved by Newton-Krylov methods. For steady state problems, only one Newton step is performed, because the time plays only the role of a relaxation parameter and there is no need to be accurate in each time step. However, for instationary problems several Newton steps are needed to maintain the accuracy in each time step. In recent work by Steiner et al. [69, 68], it was possible to design a break condition for the Newton methods that relies on the threshold value of the multiscale method.

To improve the efficiency of the solution of the nonlinear system one might employ the multilevel structure of the underlying grid hierarchy in the multiscale analysis similar to adaptive multigrid techniques such as Brandt's so-called multilevel adaptive technique (MLAT), cf. [16, 17], that is an adaptive generalization of the full approximation scheme (FAS). The efficiency of these methods crucially relies on the proper choice of problem-dependent transfer and relaxation operators. First investigations in [56] and [57] for unsteady state and steady state flow problems, respectively, show that opposite to classical adaptive multigrid schemes we may employ the multiresolution analysis using biorthogonal wavelets to define the restriction and prolongation operators. Since the underlying problem is nonlinear, the FAS [16] is used for the coarse grid correction. Further investigations are needed to fully employ the high potential of the multiresolution analysis when applying it directly to the discrete evolution equations arising from the finite volume discretization rather than just using it as a data compression tool for the set of discrete cell data.

(ii) By the implicit time discretization, the data in all cells are coupled and, hence, an information could propagate throughout the entire computational domain in one time step. Since the prediction strategy in Section 5.3 relies on the fact that the information propagates at most by one cell, the prediction has to be adjusted. Typ-

ically, for convection-dominated problems such as compressible fluid flow at high Reynolds numbers the influence of a local perturbation decays rapidly in space and stays more or less local. In [11], a heuristic approach has been developed for viscous problems where the parameter q in Harten's strategy has been coupled with the viscosity parameter. However, a rigorous mathematical justification of its reliability in the sense of the condition (16) is still missing.

Trend 3: Time step adaptation. The crux of adaptive multiresolution schemes is the multiresolution analysis of data corresponding to an arbitrary but fixed time. Therefore the local time variation is not directly accessible from the analysis of the spatial variation. In recent years, there have been several attempts to develop time adaptive scheme where the time step is controlled. This is not to be confused with multilevel time stepping as presented in Section 5.4.

A possible strategy has been investigated by Ferm and Lotstedt [36] based on time step control strategies for ODEs. Here a Runge-Kutta-Fehlberg method is applied to the semi-discretized flow equations by which the local spatial and temporal errors are estimated. These errors determine the local stepsize in time and space. Later on, this idea was also embedded in fully adaptive multiresolution finite volume schemes, cf. [30]. Alternatively, Kröner and Ohlberger [48] based their space-time adaptivity upon Kuznetsov-type a-posteriori L_1-error-estimates for scalar conservation laws.

More recently, explicit and implicit finite volume solvers on adaptively refined meshes have been coupled with adjoint techniques to control the time stepsizes for the solution of weakly instationary compressible inviscid flow problems like transonic flight. These can be considered perturbations of stationary flows. While time accuracy is still needed to study phenomena like aero-elastic interactions, large time steps may be possible when the perturbations have passed. Here the time step control is based on a space-time-splitting of the adjoint error representation, cf. [33, 5, 6]. In [68, 69] the multiscale-based grid adaptation was combined with these adjoint techniques to solve efficiently instationary problems. The advantage of this space adaptive method is that it also provides an efficient break condition for the Newton iteration in the implicit time integration.

Trend 4: Parallelization. Although multiscale-based grid adaptation leads to a significant reduction of the computational complexity (CPU time and memory) in comparison to computations on uniform meshes, this is not sufficient to perform 3D computations for complex geometries efficiently. In addition, we need parallelization techniques in order to further reduce the computational time to an affordable order of magnitude. On a distributed memory architecture, the performance of a parallelized code crucially depends on the load-balancing and the interprocessor communication. Since the underlying adaptive grids are unstructured due to hanging nodes, this task cannot be considered trivial. For this purpose, graph partitioning methods are frequently employed using the Metis software [47, 46]. An alternative approach is based on space-filling curves, cf. [71]. Here the basic idea is to map level-dependent multiindices identifying the cells in a dyadic grid hierarchy of nested grids to a onedimensional line. The interval is then split into different parts each containing the same number of entries. In the context of adaptive multiresolu-

tion schemes both the graph-partitioning and the space-filling curve approach have been used, cf. [61, 62] and [18, 4], respectively.

Nowadays more and more powerful parallel hardware architectures based on clusters of shared memory machines are being developed. Therefore the above concepts have to be reconsidered. In order to fully employ the power of the machines, a redesign of algorithms and data structures seems to be indispensable taking into account issues such as caching and threading.

Trend 5: Turbulence Modeling. The potential of the multiresolution analysis is not only restricted to pure data analysis but can be used, for instance, to model turbulent flow. The inherent problem of simulating turbulent flows comes from the number of degrees of freedom needed to resolve turbulent structures. This number is proportional to $Re^{9/4}$ and becomes dramatically large with increasing Reynolds number Re, e.g. in aerodynamics $Re \sim 10^6$, that makes a direct numerical simulation (DNS) impossible in many applications. In general, the interest is not in the fully resolved turbulent flow field but in some macroscopic quantities such as lift and drag coefficients. At the macroscale the quantities can be resolved. However, they are influenced by the non-resolved fluctuations. Typically, the influence of the fluctuations is described using some algebraic models, the Reynolds-averaged Navier-Stokes equations (RANS) or large eddy simulations (LES). Alternatively, the coherent vortex simulation (CVS) developed by Farge et al. [35, 64, 34] for incompressible flows has been designed to compute this problem with a reduced number of degrees of freedom. This methodology is based on the wavelet representation of the vorticity. The basic idea is to extract the coherent vortex structures from the noise which will then be modeled to compute the flow evolution.

Up to now, it is not apriorily known whether the choice of degrees of freedom corresponding to the resolved macroscale is sufficient to capture adequately the influence of the small scales on the macroscale. Using multiresolution techniques in combination with recent quantitative estimates for the action of the nonlinearity on different scales of the flow field, cf. [22, 23], seem to offer a promising possibility to investigate more rigorously the effect of the fluctuations on the coarse scales. In particular, it will be interesting to adjust the local scale of resolution adaptively at run time instead of fixing it before starting the computation. Work in this regard is done in [29].

Acknowledgements The author would like to express his deepest gratitude to Wolfgang Dahmen who has been supporting and inspiring the author's scientific work for many years.

References

1. S. Andreae, J. Ballmann, and S. Müller. Wave processes at interfaces. In G. Warnecke, editor, *Analysis and numerics for conservation laws*, pages 1–25. Springer, Berlin, 2005.
2. A. Baeza and P. Mulet. Adaptive mesh refinement techniques for high-order shock capturing schemes for multi-dimensional hydrodynamic simulations. *Int. Journal for Numerical Methods in Fluids*, 52(4):455–471, 2006.

3. J. Ballmann. *Flow Modulation and Fluid-Structure-Interaction at Airplane Wings*, volume 84 of *Numerical Notes on Fluid Mechanics*. Springer Verlag, 2003.
4. J. Ballmann, K. Brix, W. Dahmen, Ch. Hohn, S. Mogosan, S. Müller, and G. Schieffer. Parallel and adaptive methods for fluid-structure-interactions. Numerical Notes on Fluid Mechanics, 2009. Submitted.
5. R. Becker and R. Rannacher. A feed-back approach to error control in finite element methods: Basic analysis and examples. *East-West J. Num. Math.*, 4:237–264, 1996.
6. R. Becker and R. Rannacher. An optimal control approach to a posteriori error estimation in finite element methods. *Acta Numer.*, 10:1–102, 2001.
7. J. Bell, M.J. Berger, J. Saltzman, and M. Welcome. Three-dimensional adaptive mesh refinement for hyperbolic conservation laws. *SIAM J. Sci. Comput.*, 15(1):127–138, 1994.
8. M.J. Berger and P. Colella. Local adaptive mesh refinement for shock hydrodynamics. *J. Comp. Physics*, 82:64–84, 1989.
9. M.J. Berger and R.J. LeVeque. Adaptive mesh refinement using wave-propagation algorithms for hyperbolic systems. *SIAM J. Numer. Anal.*, 35(6):2298–2316, 1998.
10. M.J. Berger and J. Oliger. Adaptive mesh refinement for hyperbolic partial differential equations. *J. Comp. Physics*, 53:484–512, 1984.
11. B. Bihari. Multiresolution schemes for conservation laws with viscosity. *J. Comp. Phys.*, 123(1):207–225, 1996.
12. B. Bihari and A. Harten. Multiresolution schemes for the numerical solution of 2–D conservation laws I. *SIAM J. Sci. Comput.*, 18(2):315–354, 1997.
13. F. Bramkamp. *Unstructured h-Adaptive Finite-Volume Schemes for Compressible Viscous Fluid Flow*. PhD thesis, RWTH Aachen, 2003. http://darwin.bth.rwth-aachen.de/opus3/volltexte/2003/725/03_255.pdf.
14. F. Bramkamp, B. Gottschlich-Müller, M. Hesse, Ph. Lamby, S. Müller, J. Ballmann, K.-H. Brakhage, and W. Dahmen. *H*-adaptive Multiscale Schemes for the Compressible Navier–Stokes Equations — Polyhedral Discretization, Data Compression and Mesh Generation. In J. Ballmann, editor, *Flow Modulation and Fluid-Structure-Interaction at Airplane Wings*, volume 84 of *Numerical Notes on Fluid Mechanics*, pages 125–204. Springer, 2003.
15. F. Bramkamp, Ph. Lamby, and S. Müller. An adaptive multiscale finite volume solver for unsteady an steady state flow computations. *J. Comp. Phys.*, 197(2):460–490, 2004.
16. A. Brandt. Multi-level adaptive solutions to boundary-value problems. *Math. Comp.*, 31:333–390, 1977.
17. A. Brandt. Multi-level adaptive techniques (mlat) for partial differential equations: Ideas and software. In *Mathematical software III, Proc. Symp., Madison 1977*, pages 277–318, 1977.
18. K. Brix, S. Mogosan, S. Müller, and G. Schieffer. Parallelization of multiscale-based grid adaptation using space-filling curves. IGPM–Report 299, RWTH Aachen, 2009.
19. R. Bürger, R. Ruiz, and K. Schneider. Fully adaptive multiresolution schemes for strongly degenerate parabolic equations with discontinuous flux. *J. Eng. Math.*, 60(3-4):365–385, 2008.
20. R. Bürger, R. Ruiz, K. Schneider, and M.A. Sepulveda. Fully adaptive multiresolution schemes for strongly degenerate parabolic equations in one space dimension. *ESAIM, Math. Model. Numer. Anal.*, 42(4):535–563, 2008.
21. J.M. Carnicer, W. Dahmen, and J.M. Peña. Local decomposition of refinable spaces and wavelets. *Appl. Comput. Harmon. Anal.*, 3:127–153, 1996.
22. A. Cohen, W. Dahmen, and R. DeVore. Adaptive wavelet schemes for nonlinear variational schemes. *Numer. Anal.*, 41(5):1785–1823, 2003.
23. A. Cohen, W. Dahmen, and R. DeVore. Sparse evaluation of compositions of functions using multiscale expansions. *SIAM J. Math. Anal.*, 35(2):279–303, 2003.
24. A. Cohen, I. Daubechies, and J. Feauveau. Bi–orthogonal bases of compactly supported wavelets. *Comm. Pure Appl. Math.*, 45:485–560, 1992.
25. A. Cohen, S.M. Kaber, S. Müller, and M. Postel. Fully Adaptive Multiresolution Finite Volume Schemes for Conservation Laws. *Math. Comp.*, 72(241):183–225, 2003.
26. A. Cohen, S.M. Kaber, and M. Postel. Multiresolution Analysis on Triangles: Application to Gas Dynamics. In G. Warnecke and H. Freistühler, editors, *Hyperbolic Problems: Theory, Numerics, Applications*, pages 257–266. Birkhäuser, 2002.

27. F. Coquel, Q.L. Nguyen, M. Postel, and Q.H. Tran. Local time stepping applied to implicit-explicit methods for hyperbolic systems. *SIAM Multiscale Modeling and Simulation*, 2009. Accepted for publication.
28. F. Coquel, M. Postel, N. Poussineau, and Q.H. Tran. Multiresolution technique and explicit-implicit scheme for multicomponent flows. *J. Numer. Math.*, 14:187–216, 2006.
29. W. Dahmen and S. Müller. Multiscale techniques for high-resolved vortex strcutures, 2008. DFG project *Multiresolution and Adaptive Methods for Convection-Dominated Problems*, http://www.sfbtr40.de/index.php?option=com_content&view=category&layout=blog&id=34&Itemid=58&lang=en
30. M. Domingues, O. Roussel, and K. Schneider. On space-time adaptive schemes for the numerical solution of partial differential equations. *ESAIM: Proceedings*, 16:181–194, 2007.
31. R. Donat. Using Harten's multiresolution framework on existing high resolution shock capturing schemes, 2009. Presentation at Workshop on *Multiresolution and Adaptive Methods for Convection-Dominated Problems*, http://www.ann.jussieu.fr/mamcdp09/slides/RosaDonatMAMCDP09.pdf.
32. J. Edwards and M.S. Liou. Low-diffusion flux-splitting methods for flows at all speeds. *AIAA Journal*, 36:1610–1617, 1998.
33. K. Eriksson and C. Johnson. Adaptive finite element methods for parabolic problems. IV. Nonlinear problems. *SIAM J. Numer. Anal.*, 32:1729–1749, 1995.
34. M. Farge and K. Schneider. Coherent vortex simulation (cvs), a semi-deterministic turbulence model using wavelets. *Turbulence and Combustion*, 66(4):393–426, 2001.
35. M. Farge, K. Schneider, and N. Kevlahan. Non-gaussianity and coherent vortex simulation for two-dimensional turbulence using an orthogonal wavelet basis. *Phys. Fluids*, 11(8):2187–2201, 1999.
36. L. Ferm and P. Lötstedt. Space-time adaptive solution of first order PDEs. *J. Sci. Comput.*, 26(1):83–110, 2006.
37. B. Gottschlich–Müller. *Multiscale Schemes for Conservation Laws*. PhD thesis, RWTH Aachen, 1998.
38. A. Harten. Discrete multi–resolution analysis and generalized wavelets. *J. Appl. Num. Math.*, 12:153–193, 1993.
39. A. Harten. Adaptive multiresolution schemes for shock computations. *J. Comp. Phys.*, 115:319–338, 1994.
40. A. Harten. Multiresolution algorithms for the numerical solution of hyperbolic conservation laws. *Comm. Pure Appl. Math.*, 48(12):1305–1342, 1995.
41. A. Harten. Multiresolution representation of data: A general framework. *SIAM J. Numer. Anal.*, 33(3):1205–1256, 1996.
42. R. Hartmann and R. Rannacher. Adaptive FE-methods for conservation laws. In G. Warnecke and H. Freistühler, editors, *Hyperbolic Problems: Theory, Numerics, Applications*, pages 495–504. Birkhäuser, 2002.
43. P. Houston, J.A. Mackenzie, E. Süli, and G. Warnecke. A posteriori error analysis for numerical approximations of Friedrichs systems. *Numer. Math.*, 82:433–470, 1999.
44. N. Hovhannisyan and S. Müller. On the stability of fully adaptive multiscale schemes for conservation laws using approximate flux and source reconstruction strategies. IGPM–Report 284, RWTH Aachen, 2008. Accepted for publication in IMA Journal of Numerical Analysis.
45. J. Jeong and F. Hussain. On the identification of a vortex. *Journal of Fluid Mechanics*, 285:69–94, 1995.
46. G. Karypis and V. Kumar. Multilevel algorithms for multi-constraint graph partitioning. *Supercomputing*, 1998.
47. G. Karypis and V. Kumar. A parallel algorithm for multilevel graph partitioning and sparse matrix ordering. *Journal of Parallel and Distributed Computing*, 48:71–85, 1998.
48. D. Kröner and M. Ohlberger. A posteriori error estimates for upwind finite volume schemes for nonlinear conservation laws in multidimensions. *Math. Comp.*, 69(229):25–39, 2000.
49. S.N. Kruzhkov. First order quasilinear equations with several space variables. *Math. USSR Sb.*, 10:217–243, 1970.

50. N.N. Kuznetsov. The weak solution of the Cauchy problem for a multi–dimensional quasilinear equation. *Mat. Zametki*, 2:401–410, 1967. In Russian.
51. Ph. Lamby. *Parametric Multi-Block Grid Generation and Application To Adaptive Flow Simulations*. PhD thesis, RWTH Aachen, 2007. http://darwin.bth.rwth-aachen.de/opus3/volltexte/2007/1999/pdf/Lamby_Philipp.pdf.
52. Ph. Lamby, R. Massjung, S. Müller, and Y. Stiriba. Inviscid flow on moving grids with multiscale space and time adaptivity. In *Numerical Mathematics and Advanced Applications: Proceedings of Enumath 2005 the 6th European Conference on Numerical Mathematics and Advanced Mathematics*, pages 755–764. Springer, 2006.
53. Ph. Lamby, S. Müller, and Y. Stiriba. Solution of shallow water equations using fully adaptive multiscale schemes. *Int. Journal for Numerical Methods in Fluids*, 49(4):417–437, 2005.
54. S. Müller. *Adaptive Multiscale Schemes for Conservation Laws*, volume 27 of *Lecture Notes on Computational Science and Engineering*. Springer, 2002.
55. S. Müller, Ph. Helluy, and J. Ballmann. Numerical simulation of a single bubble by compressible two-phase fluids. *Int. Journal for Numerical Methods in Fluids*, 2009. DOI 10.1002/fld.2033.
56. S. Müller and Y. Stiriba. Fully adaptive multiscale schemes for conservation laws employing locally varying time stepping. *Journal for Scientific Computing*, 30(3):493–531, 2007.
57. S. Müller and Y. Stiriba. A multilevel finite volume method with multiscale-based grid adaptation for steady compressible flow. *Journal of Computational and Applied Mathematics, Special Issue: Emergent Applications of Fractals and Wavelets in Biology and Biomedicine*, 227(2):223–233, 2009. DOI 10.1016/j.cam.2008.03.035.
58. S. Osher and R. Sanders. Numerical approximations to nonlinear conservation laws with locally varying time and space grids. *Math. Comp.*, 41:321–336, 1983.
59. S.A. Pandya, S. Venkateswaran, and T.H. Pulliam. Implementation of preconditioned dual-time procedures in overflow. *AIAA Paper 2003-0072*, 2003.
60. J.J. Quirk. *An adaptive grid algorithm for computational shock hydrodynamics*. PhD thesis, Cranfield Institute of Technology, 1991.
61. O. Roussel and K. Schneider. Adaptive multiresolution method for combustion problems: Application to flame ball-vortex interaction. *Computers and Fluids*, 34(7):817–831, 2005.
62. O. Roussel and K. Schneider. Numerical studies of spherical flame structures interacting with adiabatic walls using an adaptive multiresolution scheme. *Combust. Theory Modelling*, 10(2):273–288, 2006.
63. O. Roussel, K. Schneider, A. Tsigulin, and H. Bockhorn. A conservative fully adaptive multiresolution algorithm for parabolic PDEs. *J. Comp. Phys.*, 188(2):493–523, 2003.
64. K. Schneider and M. Farge. Numerical simulation of a mixing layer in an adaptive wavelet basis. *C.R. Acad. Sci. Paris Série II b*, 328:263–269, 2001.
65. W. Schröder. *Flow Modulation and Fluid-Structure-Interaction at Airplane Wings II*. Numerical Notes on Fluid Mechanics. Springer Verlag, 2009. In preparation.
66. T. Sonar, V. Hannemann, and D. Hempel. Dynamic adaptivity and residual control in unsteady compressible flow computation. *Math. and Comp. Modelling*, 20:201–213, 1994.
67. T. Sonar and E. Süli. A dual graph–norm refinement indicator for finite volume approximations of the Euler equations. *Numer. Math.*, 78:619–658, 1998.
68. Ch. Steiner. *Adaptive timestepping for conservation laws via adjoint error representation*. PhD thesis, RWTH Aachen, 2008. http://darwin.bth.rwth-aachen.de/opus3/volltexte/2009/2679/.
69. Ch. Steiner, S. Müller, and S. Noelle. Adaptive timestep control for weakly instationary solutions of the Euler equations. IGPM–Report 292, RWTH Aachen, 2009.
70. Ch. Steiner and S. Noelle. On adaptive timestepping for weakly instationary solutions of hyperbolic conservation laws via adjoint error control. *Communications in Numerical Methods in Engineering*, 2008. Accepted for publication.
71. G. Zumbusch. *Parallel multilevel methods. Adaptive mesh refinement and loadbalancing*. Advances in Numerical Mathematics. Teubner, Wiesbaden, 2003.